Auxiliary Material

GPS-derived interseismic coupling on the subduction and seismic hazards in the Atacama region, Chile

1 Detail of GPS data set

We combine data from 17 different surveys conducted every six months from May 2004 to December 2011, and once in 2012. Because the network is large and composed of 80 benchmarks, only parts of

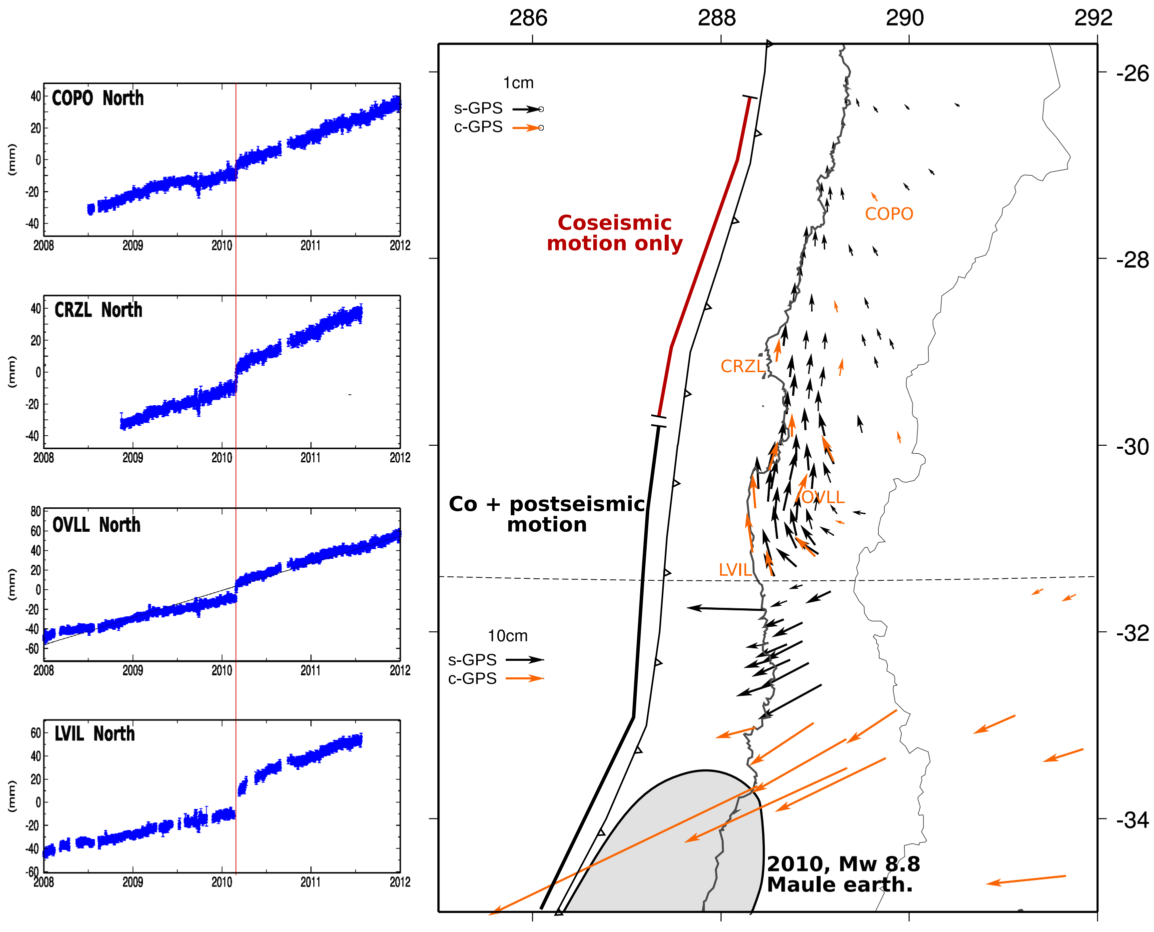

Figure 1: Left : time series of four continuous stations of our Norte Chico network imaging the coseismic and postseismic signal associated to Maule event on the North component, if so. Right : coseismic jump measured on permanent stations by Vigny et al. (2011) (orange vectors), and interpolated jump on each benchmark (black arrows).

it were measured during the surveys (see details of the measurements on table 2). We process each survey independently and calculate the repeatabilities on each component of the benchmarks positions (table 5) : repeatabilities on the horizontal components are hardly higher than 2 mm/yr, but they range generally between 3 and 7 mm/yr for the vertical component due to tropospheric effects.

To combine all of these surveys and get purely interseismic velocities, we reject the positions that were affected by either coseismic or postseismic motion south of La Serena (30°S) since most of the benchmarks therein were sufficiently measured before 2010 to obtain accurate interseismic velocities. We started measuring the central part of the network (from La Serena to Vallenar, 30°S to 28.5°S) in 2008 and the Atacama network (28.5°S to 25.5°S) since 2010. Therefore, we calculate the theoretical coseismic jumps associated with the Maule earthquake on the benchmarks of the central network in order to combine the pre-Maule surveys with the post-Maule ones. We use the published coseismic jumps on permanent GPS stations of the French-Chilean network (Vigny et al., 2011) and estimate the jump on each benchmark by interpolation of those data (figure 1). Finally, we apply these coseismic motions in our global combination (table 2). We used nine continuous stations from IGS (International GNSS Service), RAMSAC (Red Argentina de Monitoreo Satelital Continuo) or RBMC (Rede Brasileira de Monitoramento Continuo) networks to define the stable South America, and we fix their horizontal velocities to the ITRF08 estimates (see table 2 and figure 2, Altamimi et al., 2007). Vertical velocities from these fiducial stations were also used to define the reference frame but their weight is decreased ten times compare to the well constrained horizontal velocities. We then rotate

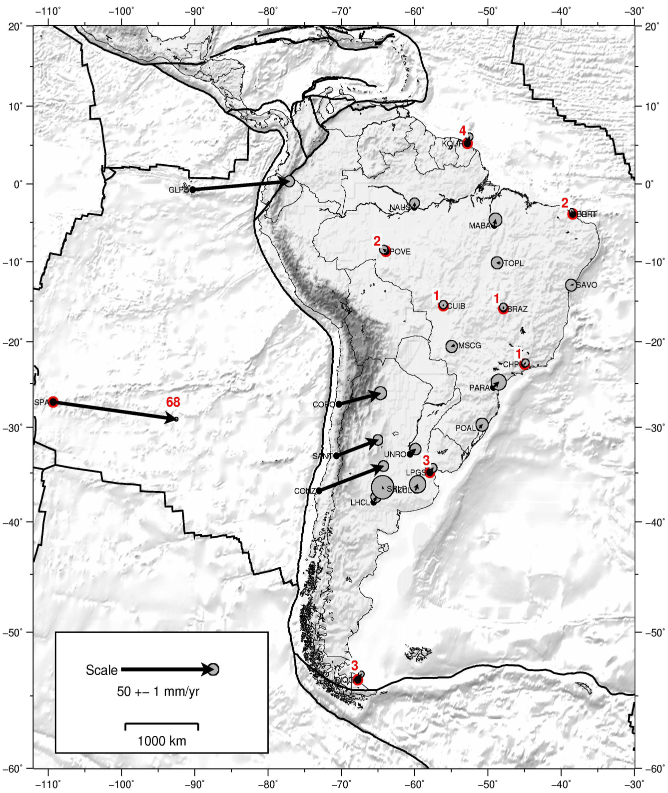

Figure 2: Large scale network and far field velocities. Dots show locations of GPS stations. Arrows depict their horizontal velocities with respect to a reference frame fixed on the South-America plate tied by the red-dot stations. Bold numbers aside the arrows indicate the velocity in mm/yr. Ellipses depict the region of 99% confidence.

the horizontal interseismic velocities into the stable South America reference frame defined by the NNR-Nuvel1A pole (25.4°S, 124.6°S, 0.11°/Myr) (tables 1 and 2, DeMets, 1994).

We combined our new data set with the older CAP and SAGA velocities (Brooks, 2003; Khazaradze, 2003). We rotate them in the same reference frame, i.e. the South American plate defined by NNR-Nuvel1A. To do so, we apply the poles published by Métois et al. (2012) to each data set, in order to share a common reference frame.

2 Vertical data set

It is unusual to use vertical velocities derived from campaign measurements since they can not be easily corrected from seasonal variations or meteorological phenomenon that can deeply impact the overall trend. Furthermore, because the vertical velocities of fiducial stations are often given a lower weight than the horizontal data in the GLORG procedure to define the reference frame (see section 1), the vertical velocities over the network can change by several mm/yr depending on the parameters used to built the stable South America. However, we think that our data provide sufficiently long time-series to get the big picture of the vertical deformation. We compare these vertical velocities with the ones calculated using continuous time-series that are being analysed and find in general a good agreement considering uncertainties of ±2mm/yr. Therefore, these data should be used, but with precaution, keeping in mind that the formal errors given in table 3 may be largely underestimated (there is no estimation of colored noise or long-term biases). Future work on continuous time-series will precise the overall vertical motion of the margin.

We selected the more reliable vertical velocities based on the quality criteria detailed by Métois et al. (2012). We rejected the velocities based on less than 2-year time span measurements, less than 3 distinct measurements, the velocities with uncertainties larger than 4.5 mm/yr or with normalized RMS (Root Mean Square) greater than 2, unrealistic high velocities (uplift larger than 10 mm/yr for Andean sites), and velocities from survey sites that differ significantly from those of nearby cGPS stations (see table 3).

SITE	Position		Velocity-ITRF08		Velocity-NNR		Uncertainties		r
	Lon.	Lat.	Vlon	Vlat	Vlon	Vlat	σ_{lon}	σ_{lat}	
3CRX	289.068	-29.376	18.65	18.96	20.01	10.06	1.32	1.32	-0.009
ABOL	288.893	-28.967	25.52	17.51	26.93	8.63	1.22	1.22	-0.010
AGRD	288.946	-29.500	16.93	20.26	18.26	11.37	1.32	1.32	-0.009
AGUA	289.193	-30.982	21.34	17.81	22.48	8.89	1.11	1.11	-0.010
ALUM	293.403	-27.323	-0.01	10.86	1.96	1.49	1.97	1.97	-0.002
ANDA	288.930	-30.278	19.27	19.26	20.49	10.37	0.90	0.91	-0.015
ATOR	289.045	-29.638	20.07	19.79	21.39	10.89	1.22	1.21	-0.010
BARQ	289.121	-27.514	22.89	18.49	24.52	9.58	1.50	1.49	-0.009
BATF	320.257	-17.555	-10.03	13.35	-5.33	2.35	1.32	1.35	-0.011
BING	289.141	-27.134	26.93	16.46	28.62	7.55	1.47	1.47	-0.009
BSAR	288.589	-28.816	29.45	20.90	30.86	12.05	1.21	1.21	-0.010
BSJL	288.662	-30.687	20.96	17.64	22.10	8.79	0.91	0.91	-0.016
CANG	288.824	-28.277	27.04	17.92	28.54	9.05	1.99	1.99	-0.008
CATA	294.226	-28.471	-1.18	13.32	0.71	3.87	1.98	1.98	-0.002
CENT	288.793	-30.962	21.85	18.43	22.96	9.56	0.90	0.91	-0.016
CHAN	288.972	-30.897	21.33	18.28	22.46	9.39	0.91	0.91	-0.015
CHAP	289.500	-29.853	16.67	16.42	18.00	7.47	0.91	0.91	-0.015
CHAR	289.339	-26.369	27.77	16.52	29.58	7.59	1.48	1.48	-0.010
CHIN	288.877	-31.488	21.72	15.61	22.76	6.73	1.29	1.29	-0.007
CHIP	288.786	-31.115	23.34	18.83	24.43	9.96	0.95	0.95	-0.015
CHR1	289.469	-26.357	26.88	15.01	28.70	6.06	1.47	1.47	-0.008
CMOR	289.204	-30.205	18.77	19.69	20.02	10.77	1.24	1.24	-0.006
CNFL	288.711	-31.672	21.98	16.56	22.98	7.70	1.29	1.29	-0.008

COGO	289.025	-31.153	21.27	17.32	22.37	8.42	1.06	1.06	-0.012
CONA	289.850	-28.975	19.09	15.40	20.57	6.41	1.49	1.48	-0.010
COP2	289.177	-27.357	25.00	18.03	26.66	9.12	1.48	1.48	-0.010
COP3	289.317	-27.358	23.38	18.07	25.05	9.14	1.48	1.48	-0.011
COP5	289.984	-27.271	19.48	14.33	21.21	5.33	1.50	1.49	-0.010
CTAL	288.330	-30.929	27.30	22.05	28.38	13.23	0.79	0.79	-0.021
CZBA	288.857	-28.063	21.57	18.51	23.10	9.63	2.03	2.01	-0.010
DGAL	289.986	-26.387	23.94	12.19	25.79	3.19	1.52	1.54	-0.010
DOME	289.114	-28.959	24.22	16.57	25.64	7.66	1.22	1.21	-0.009
EALM	288.570	-31.413	22.29	17.29	23.32	8.45	1.07	1.06	-0.011
EMAN	288.815	-30.175	18.39	18.89	19.62	10.02	0.90	0.91	-0.015
ESAU	288.316	-30.511	22.69	20.69	23.83	11.88	0.79	0.79	-0.021
ESPI	288.545	-31.220	23.95	18.93	25.00	10.09	0.90	0.91	-0.016
ETRA	289.714	-28.865	18.87	18.87	20.35	9.90	1.49	1.48	-0.001
FREI	288.980	-28.564	26.55	16.99	28.02	8.10	1.32	1.32	-0.009
FRTN	289.555	-28.522	21.49	17.87	23.01	8.91	1.52	1.51	-0.007
FUND	289.149	-30.383	17.85	19.06	19.07	10.15	0.91	0.91	-0.016
HERA	288.621	-29.998	18.66	18.59	19.90	9.74	0.90	0.91	-0.015
HGRT	288.684	-28.944	25.14	20.29	26.53	11.43	1.21	1.21	-0.010
HORN	288.688	-29.679	19.58	19.28	20.87	10.42	1.22	1.22	-0.010
HUA0	288.778	-28.478	32.18	18.49	33.65	9.62	1.52	1.52	-0.008
INCA	288.935	-29.242	19.74	18.53	21.11	9.64	1.22	1.22	-0.010
LAMB	288.884	-29.830	16.09	19.74	17.37	10.86	2.16	2.14	-0.008
LAPU	290.273	-27.109	19.87	12.33	21.64	3.29	2.01	2.00	-0.008
LCAN	288.560	-30.789	21.22	18.16	22.34	9.32	0.95	0.95	-0.014
LCHO	288.739	-29.277	19.59	19.77	20.94	10.91	1.32	1.32	-0.009
LISL	288.989	-31.061	21.58	17.85	22.69	8.96	1.21	1.20	-0.006
LMOL	289.542	-30.742	18.25	17.09	19.45	8.14	0.91	0.91	-0.015
LPER	288.749	-30.365	17.75	20.15	18.94	11.29	0.91	0.91	-0.016
MPAT	288.987	-30.702	20.61	19.09	21.77	10.20	1.01	1.01	-0.014
NIPA	288.534	-30.469	20.71	18.31	21.87	9.47	1.11	1.11	-0.011
OVEJ	288.806	-31.293	21.60	18.53	22.66	9.66	0.90	0.91	-0.016
PACH	288.405	-30.457	21.01	17.82	22.16	9.00	0.95	0.95	-0.014
PALD	288.394	-30.309	23.86	21.37	25.03	12.55	2.14	2.13	-0.007
PCHO	288.542	-29.254	23.06	20.31	24.40	11.47	1.21	1.21	-0.010
PIDN	288.786	-30.815	21.66	18.48	22.79	9.61	0.90	0.91	-0.016
PLTT	289.200	-26.881	26.70	16.23	28.43	7.31	1.50	1.48	-0.011
PNAZ	289.346	-26.148	27.10	14.98	28.94	6.05	1.48	1.48	-0.009
POAL	308.880	-30.074	-0.99	12.10	1.98	1.51	1.11	1.10	0.000
POBR	288.496	-30.591	20.74	18.79	21.88	9.95	0.90	0.91	-0.016
POTR	290.542	-26.374	23.81	12.20	25.71	3.13	1.48	1.48	-0.008
PPLY	289.649	-29.180	16.63	16.90	18.06	7.93	1.27	1.25	-0.009
PTOM	288.428	-31.532	24.53	17.51	25.53	8.68	0.91	0.91	-0.016
PVEJ	289.060	-27.341	25.53	16.90	27.18	8.00	1.47	1.47	-0.010
SALD	289.658	-26.423	26.44	15.31	28.27	6.34	1.48	1.48	-0.009
SFLX	289.542	-28.933	20.35	16.23	21.81	7.28	1.27	1.26	-0.019
SGER	289.087	-29.892	18.09	17.51	19.38	8.61	1.29	1.29	-0.008
SPED	288.606	-31.015	22.55	18.29	23.64	9.44	0.90	0.91	-0.016
TAHU	288.958	-30.477	18.93	18.47	20.12	9.58	0.90	0.91	-0.015
TINC	289.294	-26.615	26.31	15.70	28.08	6.77	1.46	1.46	-0.009
TOFO	288.762	-29.459	20.30	19.48	21.63	10.61	1.22	1.22	-0.010
TONG	288.498	-30.249	20.18	18.03	21.37	9.19	1.08	1.08	-0.002
TOT2	289.012	-27.870	20.49	18.09	22.06	9.20	1.48	1.48	-0.011
TOT3	289.115	-27.912	22.27	18.87	23.85	9.96	1.48	1.49	-0.011
TOT4	289.387	-27.977	20.82	17.28	22.41	8.34	1.49	1.49	-0.011
TOT5	289.660	-27.951	17.55	17.80	19.16	8.83	1.49	1.49	-0.009
VARI	289.250	-30.741	17.92	18.67	19.10	9.75	1.11	1.11	-0.010

Table 1: Horizontal velocities in mm/yr on our campaign network. Vlat and Vlon are given either in the ITRF 2008 reference frame (columns 3 and 4), or in the NNR-Nuvel1A South-America fixed reference frame (columns 5 and 6).

SITE	Position		Velocity-ITRF08		Velocity-NNR		Uncertainties		r
	Lon.	Lat.	Vlon	Vlat	Vlon	Vlat	σ_{lon}	σ_{lat}	
AZUL[a]	300.119	-36.767	0.27	12.19	1.65	2.20	1.47	1.46	-0.002
BRAZ*[i]	312.122	-15.947	-4.25	12.10	0.10	1.35	0.66	0.65	0.000
BRFT*[i]	321.574	-3.877	-4.96	12.95	0.22	1.93	0.62	0.60	0.050
BTON[f]	288.513	-30.263	19.33	18.13	20.52	9.29	1.19	1.19	-0.009
CEEU[b]	321.574	-3.878	-6.51	9.48	-1.33	-1.54	1.61	1.56	-0.026
CFAG[i]	291.767	-31.602	11.33	12.92	12.59	3.72	0.84	0.84	-0.017
CHPI*[i]	315.015	-22.687	-3.22	11.82	0.85	0.95	0.65	0.64	-0.007
CMBA[f]	289.001	-31.188	21.12	17.89	22.21	9.00	1.29	1.29	-0.008
CRZL[f]	288.590	-29.102	25.16	20.69	26.52	11.84	1.11	1.11	-0.013
CUIB*[b]	303.930	-15.555	-4.10	11.21	-0.13	0.93	0.70	0.70	0.001
EMAT[f]	288.337	-31.147	29.25	18.41	30.30	9.59	0.90	0.91	-0.016
GLPS[i]	269.696	-0.743	48.40	10.40	53.53	4.17	0.92	0.93	0.002
ISPA*[i]	250.656	-27.125	67.55	-5.33	67.36	-8.24	0.39	0.37	-0.108
JUNT[f]	289.906	-29.977	16.51	16.60	17.85	7.60	1.47	1.47	-0.006
KOUR*[i]	307.194	5.252	-6.15	12.77	-0.61	2.27	0.59	0.62	-0.020
LHCL[i]	294.405	-38.003	0.78	11.10	1.41	1.63	0.92	0.91	-0.017
LPGS*[i]	302.068	-34.907	-0.09	11.91	1.71	1.76	0.75	0.75	0.015
LSCH[f]	288.754	-29.908	19.02	19.19	20.28	10.32	1.19	1.19	-0.009
LVIL[f]	288.486	-31.909	23.65	17.18	24.60	8.35	0.90	0.91	-0.017
MABA[b]	310.878	-5.362	-4.44	14.15	0.52	3.45	1.15	1.14	-0.018
MSCG[b]	305.459	-20.441	-4.75	10.41	-1.15	0.02	1.03	1.03	-0.005
MTCO[b]	304.544	-10.804	-5.21	9.63	-0.79	-0.70	1.32	1.31	-0.008
MZAC[a]	291.124	-32.895	9.50	13.43	10.53	4.30	0.99	0.99	-0.014
MZAE[a]	291.850	-33.255	5.93	11.16	6.97	1.95	1.46	1.46	-0.006
NAUS[b]	299.945	-3.023	-4.84	12.63	0.15	2.65	0.88	0.86	0.004
OVLL[f]	288.796	-30.604	20.68	19.10	21.84	10.23	0.90	0.90	-0.016
PARA[b]	310.769	-25.448	-0.37	13.41	3.17	2.72	1.36	1.35	-0.007
PEDR[f]	289.311	-30.839	20.23	19.33	21.40	10.40	1.19	1.19	-0.009
PFRJ[f]	288.365	-30.675	22.93	18.02	24.05	9.20	1.19	1.19	-0.010
PORT[f]	289.870	-32.835	18.25	16.39	19.18	7.40	0.90	0.90	-0.017
POVE*[b]	296.104	-8.709	-6.05	11.29	-1.68	1.65	0.74	0.73	-0.005
RCSD[f]	288.387	-33.654	26.87	21.90	27.55	13.08	1.98	1.98	-0.004
RIOG*[i]	292.249	-53.785	3.47	11.11	1.69	1.86	0.54	0.54	0.017
ROBL[f]	288.985	-32.976	22.25	19.60	23.08	10.71	1.98	1.97	-0.004
SALU[b]	315.788	-2.593	-5.56	10.88	-0.40	-0.01	1.36	1.34	-0.032
SANT[i]	289.331	-33.150	21.74	16.43	22.58	7.50	0.90	0.90	-0.018
SAVO[b]	321.568	-12.939	-5.10	12.10	-0.15	1.08	1.00	1.02	-0.023
SILL[f]	289.261	-29.255	19.42	15.91	20.81	6.99	1.11	1.11	-0.013
SLMC[f]	289.037	-31.777	20.32	17.87	21.33	8.97	0.76	0.76	-0.024
SRLP[a]	295.720	-36.621	-1.03	9.58	-0.08	-0.02	2.00	1.99	-0.001
TERO[a]	295.743	-27.789	-2.58	13.25	-0.49	3.65	1.98	1.97	-0.002
TOLO[f]	289.194	-30.170	17.80	19.37	19.06	10.45	0.99	0.99	-0.013
TOPL[b]	311.669	-10.171	-5.87	11.87	-1.17	1.14	1.05	1.04	-0.017
TUCU[a]	294.770	-26.843	3.03	10.93	5.17	1.42	0.90	0.90	-0.010
UCOR[a]	295.806	-31.435	3.49	12.28	5.12	2.67	0.99	0.98	-0.010
UNRO[a]	299.372	-32.959	1.52	11.89	3.28	1.96	0.99	0.98	-0.008
UNSJ[a]	291.423	-31.541	9.80	13.40	11.04	4.24	1.28	1.28	-0.007
VALN[f]	288.365	-33.028	27.92	21.43	28.69	12.61	1.11	1.11	-0.013
VALL[f]	289.236	-28.572	23.95	16.73	25.44	7.81	1.32	1.32	-0.012
VBCA[a]	297.731	-38.701	2.55	12.38	3.44	2.59	1.00	0.99	-0.011
VNEV[f]	289.751	-33.354	18.06	15.60	18.90	6.62	0.90	0.90	-0.018

Table 2: Horizontal velocities in mm/yr on permanent stations used to stabilize the processing. Sites used to constrain the reference frame are marked by the * symbol. Note that only pre-Maule data from LPGS were used to constrain the reference frame. Stations are either from IGS network [i], French-Chilean network [f], RAMSAC Argentine network [a], or RBMC Brazilian network[b].

SITE	Position		Vup	σ_{up}
	Lon.	Lat.	mm/yr	
3CRX	289.068	-29.376	0.01	1.69
ABOL	288.893	-28.967	2.84	1.59
AGRD	288.946	-29.500	5.64	1.71
AGUA	289.193	-30.982	2.20	1.40
ANDA	288.930	-30.278	5.91	1.03
ANTC	288.468	-37.339	3.59	1.01
BSAR	288.589	-28.816	-7.23	1.49
BSJL	288.662	-30.687	1.37	1.17
BTON	288.513	-30.263	1.04	1.38
CENT	288.793	-30.962	8.15	1.06
CHAN	288.972	-30.897	3.17	1.07
CHAP	289.500	-29.853	7.20	1.09
CHIN	288.877	-31.488	5.86	1.75
CHIP	288.786	-31.115	7.05	1.12
CMBA	289.001	-31.188	2.36	1.54
CNFL	288.711	-31.672	2.98	1.60
COGO	289.025	-31.153	7.88	1.26
CONA	289.850	-28.975	2.11	2.44
CONS	287.588	-35.331	1.77	0.99
CONZ	286.975	-36.844	-0.02	1.00
COPO	289.662	-27.385	2.83	1.26
CRZL	288.590	-29.102	-0.55	1.21
CTAL	288.330	-30.929	-3.44	0.89
DOME	289.114	-28.959	4.72	1.52
EALM	288.570	-31.413	1.76	1.31
EMAN	288.815	-30.175	4.01	1.05
EMAT	288.337	-31.147	-2.26	1.02
ESAU	288.316	-30.511	1.66	0.89
ESPI	288.545	-31.220	2.24	1.04
ETRA	289.714	-28.865	1.08	2.52
FREI	288.980	-28.564	-0.18	1.72
FUND	289.149	-30.383	5.87	1.09
GLPS	269.696	-0.743	-4.00	1.20
HERA	288.621	-29.998	1.68	1.04
HGRT	288.684	-28.944	-3.57	1.51
HORN	288.688	-29.679	4.92	1.56
INCA	288.935	-29.242	-0.30	1.74
ISPA	250.656	-27.125	1.16	0.95
LCAN	288.560	-30.789	4.20	1.09
LCHO	288.739	-29.277	-5.22	1.68
LMOL	289.542	-30.742	3.74	1.08
LPER	288.749	-30.365	5.80	1.05
LSCH	288.754	-29.908	0.94	1.37
LVIL	288.486	-31.909	4.00	1.00
MAUL	289.179	-35.810	0.87	1.00
MPAT	288.987	-30.702	2.72	1.22
NIPA	288.534	-30.469	3.04	1.34
OVEJ	288.806	-31.293	5.23	1.06
OVLL	288.796	-30.604	5.26	0.99
PACH	288.405	-30.457	-2.52	1.09
PCHO	288.542	-29.254	-1.70	1.46
PEDR	289.311	-30.839	2.66	1.37
PFRJ	288.365	-30.675	1.59	1.37
PIDN	288.786	-30.815	4.54	1.10
POBR	288.496	-30.591	3.86	1.05
PORT	289.870	-32.835	7.28	0.98
PPLY	289.649	-29.180	8.49	2.57
PTOM	288.428	-31.532	1.90	1.08
SANT	289.331	-33.150	4.38	0.99
SFLX	289.542	-28.933	-3.12	2.30
SILL	289.261	-29.255	4.96	1.17
SJAV	288.267	-35.595	5.24	1.02
SLMC	289.037	-31.777	7.97	0.81
SPED	288.606	-31.015	3.40	1.03
TAHU	288.958	-30.477	4.00	1.08
TOFO	288.762	-29.459	1.98	1.54
TOLO	289.194	-30.170	5.81	1.10
TONG	288.498	-30.249	4.24	1.41
VALL	289.236	-28.572	2.03	1.53
VALN	288.365	-33.028	0.71	1.28
VARI	289.250	-30.741	4.08	1.37
VNEV	289.751	-33.354	3.21	0.99

Table 3: Vertical velocities in mm/yr selected on several quality criteria, for the inversion process.

SITE	04a	04b	05a	05b	06a	06b	07a	07b	08a	08b	09a	09b	10a	10b	11a	11b	12
3CRX	-	-	-	-	-	-	-	-	-	-	X	X	-	X	-	X	-
ABOL	-	-	-	-	-	-	-	-	-	X	-	X	-	X	-	X	-
AGRD	-	-	-	-	-	-	-	-	-	-	X	X	-	X	-	X	-
AGUA	-	-	-	-	X	X	X	X	X	X	-	X	-	-	-	-	-
ALUM	-	-	-	-	-	-	-	-	-	X	X	X	-	-	-	-	-
ANDA	X	X	X	X	X	X	X	X	X	X	-	X	-	-	-	-	-
ATOR	-	-	-	-	-	-	-	-	-	X	X	X	-	X	-	X	-
AZUL	-	-	-	-	-	-	-	X	X	X	X	X	-	-	-	-	-
BARQ	-	-	-	-	-	-	-	-	-	-	-	-	X	-	X	-	X
BATF	-	-	-	-	-	-	-	-	-	-	-	X	X	X	X	X	X
BING	-	-	-	-	-	-	-	-	-	-	-	-	X	-	X	-	X
BSAR	-	-	-	-	-	-	-	-	-	X	X	X	-	X	-	X	-
BSJL	X	X	X	X	X	X	X	-	-	-	-	X	-	-	-	-	-
CANG	-	-	-	-	-	-	-	-	-	-	-	-	-	-	X	-	X
CATA	-	-	-	-	-	-	-	-	-	X	X	X	-	-	-	-	-
CENT	X	X	X	X	X	X	X	X	X	X	-	X	-	-	-	-	-
CHAN	X	X	X	X	X	X	X	X	X	X	-	X	-	-	-	-	-
CHAP	X	X	X	X	X	X	X	X	X	X	-	X	-	-	-	-	-
CHAR	-	-	-	-	-	-	-	-	-	-	-	-	X	-	X	-	X
CHIN	-	-	-	-	-	-	X	X	X	X	-	X	-	-	-	-	-
CHIP	-	X	X	X	X	X	X	X	X	X	-	X	-	-	-	-	-
CHR1	-	-	-	-	-	-	-	-	-	-	-	-	X	-	X	-	X
CMOR	X	X	X	-	-	-	X	-	-	-	-	-	-	-	-	-	-
CNFL	-	-	-	-	-	-	X	X	X	X	-	X	-	-	-	-	-
COGO	X	X	X	X	X	X	X	X	X	-	-	-	-	-	-	-	-
CONA	-	-	-	-	-	-	-	-	-	X	X	X	-	X	-	-	-
COP2	-	-	-	-	-	-	-	-	-	-	-	-	X	-	X	-	X
COP3	-	-	-	-	-	-	-	-	-	-	-	-	X	-	X	-	X
COP5	-	-	-	-	-	-	-	-	-	-	-	-	X	-	X	-	X
CTAL	X	X	X	X	X	X	X	X	X	X	-	X	-	X	-	X	-
CZBA	-	-	-	-	-	-	-	-	-	-	-	-	-	-	X	-	X
DGAL	-	-	-	-	-	-	-	-	-	-	-	-	X	-	X	-	X
DOME	-	-	-	-	-	-	-	-	-	X	X	X	-	X	-	X	-
EALM	X	X	X	X	X	X	X	X	X	-	-	-	-	-	-	-	-
EMAN	X	X	X	X	X	X	X	X	X	X	-	X	-	-	-	-	-
ESAU	X	X	X	X	X	X	X	X	X	X	-	X	-	X	-	X	-
ESPI	X	X	X	X	X	X	X	X	X	X	-	X	-	-	-	-	-
ETRA	-	-	-	-	-	-	-	-	-	X	X	X	-	X	-	-	-
FREI	-	-	-	-	-	-	-	-	-	-	X	X	-	X	-	X	-
FRTN	-	-	-	-	-	-	-	-	-	-	-	X	-	X	-	X	-
FUND	X	X	X	X	X	X	X	X	X	X	-	X	-	-	-	-	-
HERA	X	X	X	X	X	X	X	X	X	X	-	X	-	-	-	-	-
HGRT	-	-	-	-	-	-	-	-	-	X	X	X	-	X	-	X	-
HORN	-	-	-	-	-	-	-	-	-	X	X	X	-	X	-	X	-
HUA0	-	-	-	-	-	-	-	-	-	-	-	X	-	X	-	X	-
INCA	-	-	-	-	-	-	-	-	-	X	X	X	-	X	-	X	-
LAMB	-	-	-	-	-	-	-	-	-	-	-	-	-	X	-	X	-
LAPU	-	-	-	-	-	-	-	-	-	-	-	-	-	-	X	-	X
LCAN	-	X	X	X	X	X	X	X	X	X	-	X	-	-	-	-	-
LCHO	-	-	-	-	-	-	-	-	-	-	X	X	-	X	-	X	-
LISL	-	-	-	-	-	X	X	X	X	X	-	X	-	-	-	-	-
LMOL	X	X	X	X	X	X	X	X	X	X	-	X	-	-	-	-	-
LPER	X	X	X	X	X	X	X	X	X	X	-	X	-	-	-	-	-
MPAT	X	X	X	X	X	X	X	X	X	X	-	-	-	-	-	-	-
NIPA	-	-	-	-	X	X	X	X	X	X	-	X	-	-	-	-	-
OVEJ	X	X	X	X	X	X	X	X	X	X	-	X	-	-	-	-	-
PACH	-	X	X	X	X	X	X	X	X	X	-	X	-	-	-	-	-
PALD	-	-	-	-	-	-	-	-	-	-	-	-	-	X	-	X	-
PCHO	-	-	-	-	-	-	-	-	-	X	X	X	-	X	-	X	-
PIDN	X	X	X	X	X	X	X	X	X	X	-	X	-	-	-	-	-
PLTT	-	-	-	-	-	-	-	-	-	-	-	-	X	-	X	-	X
PNAZ	-	-	-	-	-	-	-	-	-	-	-	-	X	-	X	-	X
POAL	-	-	-	-	X	X	X	X	X	X	X	X	-	-	-	-	-
POBR	X	X	X	X	X	X	X	X	X	X	-	X	-	-	-	-	-
POTR	-	-	-	-	-	-	-	-	-	-	-	-	X	-	X	-	X
PPLY	-	-	-	-	-	-	-	-	-	X	X	X	-	X	-	X	-
PTOM	X	X	X	X	X	X	X	X	X	X	-	X	-	-	-	-	-
PVEJ	-	-	-	-	-	-	-	-	-	-	-	-	X	-	X	-	X
SALD	-	-	-	-	-	-	-	-	-	-	-	-	X	-	X	-	X
SFLX	-	-	-	-	-	-	-	-	-	X	X	X	-	X	-	X	-
SGER	-	-	-	-	-	-	X	X	X	X	X	X	-	-	-	-	-
SPED	X	X	X	X	X	X	X	X	X	X	-	X	-	-	-	-	-
TAHU	X	X	X	X	X	X	X	X	X	X	-	X	-	-	-	-	-
TINC	-	-	-	-	-	-	-	-	-	-	-	-	X	-	X	-	X
TOFO	-	-	-	-	-	-	-	-	-	X	X	X	-	X	-	X	-
TONG	X	X	X	X	X	X	X	X	X	-	-	-	-	-	-	-	-
TOT2	-	-	-	-	-	-	-	-	-	-	-	-	X	-	X	-	X
TOT3	-	-	-	-	-	-	-	-	-	-	-	-	X	-	X	-	X
TOT4	-	-	-	-	-	-	-	-	-	-	-	-	X	-	X	-	X
TOT5	-	-	-	-	-	-	-	-	-	-	-	-	X	-	X	-	X
VARI	-	-	-	-	X	X	X	X	X	X	-	X	-	-	-	-	-

Table 4: Table of measurement for each campaign since 2004.

Campaign	04a	04b	05a	05b	06a	06b	07a	07b	08a	08b	09a	09b	10a	10b	11a	11b	12
North	1.4	1.2	1.2	2.0	0.7	1.3	0.9	1.4	0.8	1.4	1.1	1.2	1.0	1.3	0.9	1.2	0.8
East	1.4	1.6	2.6	2.4	1.6	1.9	1.4	2.4	1.2	1.5	1.5	1.7	1.6	2.0	1.7	2.5	1.3
Vert	4.4	4.8	5.3	7.3	3.2	5.4	3.8	6.2	4.0	5.2	4.3	4.7	4.8	4.6	3.5	4.3	4.5

Table 5: Repeatability for each campaign on North, East and vertical components.

SITE	Lon.	Lat.	North	East	Up
3CRX	289.068	-29.376	-6.67	-0.79	-1.6
ABOL	288.893	-28.967	-6.44	-0.39	-4.7
AGRD	288.946	-29.500	-7.17	-0.58	1.2
ATOR	289.045	-29.638	-7.17	0	2.6
BARQ	289.121	-27.514	-4.77	0.19	-2.7
BING	289.141	-27.134	-4.42	0	-2.4
BSAR	288.589	-28.816	-7.47	-0.86	-6.33
CANG	288.824	-28.277	-6.44	-0.51	-5
CHAR	289.339	-26.369	-3.06	0.39	-0.7
CHR1	289.469	-26.357	-2.64	0.86	0
COP2	289.177	-27.357	-4.53	0.25	-2.4
COP3	289.317	-27.358	-4.11	0.72	-1.8
COP5	289.984	-27.271	-2.5	1.95	-0.2
CZBA	288.857	-28.063	-6.14	-0.48	-4.6
DGAL	289.986	-26.387	-1.66	1.51	0.3
DOME	289.114	-28.959	-5.7	-0.25	-2.2
ETRA	289.714	-28.865	-3.67	1.32	0
FREI	288.980	-28.564	-6.11	0	-4.8
FRTN	289.555	-28.522	-3.64	1.35	-1.3
HGRT	288.684	-28.944	-7.59	-0.8	-6.4
HORN	288.688	-29.679	-8.03	-0.35	0
HUA0	288.778	-28.478	-6.84	-0.66	-5.5
INCA	288.935	-29.242	-7.01	-0.93	-1.3
LAPU	290.273	-27.109	-1.96	1.88	-0.5
LCHO	288.739	-29.277	-7.65	-0.82	-3.5
PCHO	288.542	-29.254	-8.41	-0.79	-5.53
PLTT	289.200	-26.881	-3.95	0.14	-1.8
PNAZ	289.346	-26.148	-2.84	0.28	-0.5
POTR	290.542	-26.374	-0.95	1.52	-0.2
PPLY	289.649	-29.180	-3.88	1.11	-0.7
PVEJ	289.060	-27.341	-4.82	-0.11	-2.9
SALD	289.658	-26.423	-2.12	1.51	0.7
SFLX	289.542	-28.933	-3.87	1.12	-1.8
TINC	289.294	-26.615	-3.39	0.37	-1.1
TOFO	288.762	-29.459	-7.67	-0.57	-1
TOT2	289.012	-27.870	-5.53	-0.1	-3.7
TOT3	289.115	-27.912	-5.25	0.25	-3.3
TOT4	289.387	-27.977	-3.9	1.32	-2.4
TOT5	289.660	-27.951	-3.25	1.74	0

Table 6: Applied coseismic jump (in mm) on North, East and Vertical direction on campain points located north of 30°S. Estimations from interpolation of coseismic jumps measured at permanent stations (Vigny et al., 2011).

3 Technical choices for modeling

The inversion procedure of the best models presented in Figure 5 of the main text is conducted using 556 independent observations to determine 356 (3-plate model with zero coupling below 80 km depth) or 353 parameters (2-plate model with zero coupling below 80 km depth). For inversion purposes, we force the rake of the backslip component to be parallel to the plate convergence velocity.

3.1 Slab geometry

In this region, the slab dip angle gradually increases from 10° at shallow depth to 25° at 45 km depth (e.g. Pardo et al., 2012; Marot et al., 2013). Between 26° and 33°S, the slab curvature reverses and the slab becomes flat below 100 km depth. We chose to fix the slab geometry rather than to invert it because of the trade-of between slab geometry and coupling depth and intensity (e.g. Chlieh et al., 2011; Métois et al., 2013). Therefore, we use a simple geometry with an homogeneous along-dip angle that slightly varies with latitude from 15° in the southern part of the network to 20° in the flat-slab area. The deep flat-slab is modeled by a 2° dipping section of the slab below 100 km depth. Anyway, being deeper than 100 km depth, the 'flat-slab" has no influence on the upper plate deformation in the elastic back-slip framework.

3.2 Sensitivity and resolution

We estimate the sensitivity of both our horizontal and vertical data sets to unit displacements on each node of the grid by summing the horizontal deformation on the whole network as suggested by Loveless and Meade (2011) (see figure 3). The "power" of our horizontal data to constrain the coupling on the interface is high from 7 km depth to more than 70 km depth in the densest part of our network, i.e. from 33°S to 26°S. Coupling deeper than 80 km depth on the interface is quite unlikely and impacts the predicted vertical deformation pattern. Thus, we impose zero coupling at nodes deeper than 80 km. The sensitivity to coupling is maximal under the Tongoy peninsula where the coast is very near the trench (70 km), and minimal under the main Cordillera, since there is a gap of measurements between the Chilean network and the Argentine one. Vertical data increase the sensitivity to coupling under the Tongoy peninsula and to deep coupling. This is consistent with the fact that the vertical elastic deformation is mainly constrained by the width of the intermediate coupling zone beneath the locked zone (Okada, 1985; McCaffrey, 2002).

We lack resolution mainly along the edges of our model (from 26°S to 25°S, and south of 33°S) and in the very shallow part of the subduction interface (from surface to $\sim$7 km depth). This is why constraining the coupling value on these nodes to 0% or 100% does not impact the nRMS of the inversion (see supp. Figure 4). Checkerboard tests presented in supp. Figure 5 confirms that our network is able to picture accurately variations of the coupling coefficient both along-strike and along-dip if located on the subduction interface between 10 and 60 km depth.

3.3 Smoothing constrains

To reduce numerical instabilities, we apply a smoothing coefficient (gradient type) along each line of nodes that reduces the lateral variability of coupling. We quantify the smoothing amount by fixing in the program the allowed roughness of the coupling distribution, given in maximal coupling variation by degree of latitude (/°). In order to avoid patchy instabilities in the deep unresolved part of the interface and following Métois et al. (2013), we impose a linear increase of the smoothing with depth equivalent to an along-dip decrease in the roughness amount. However, note that we do not impose

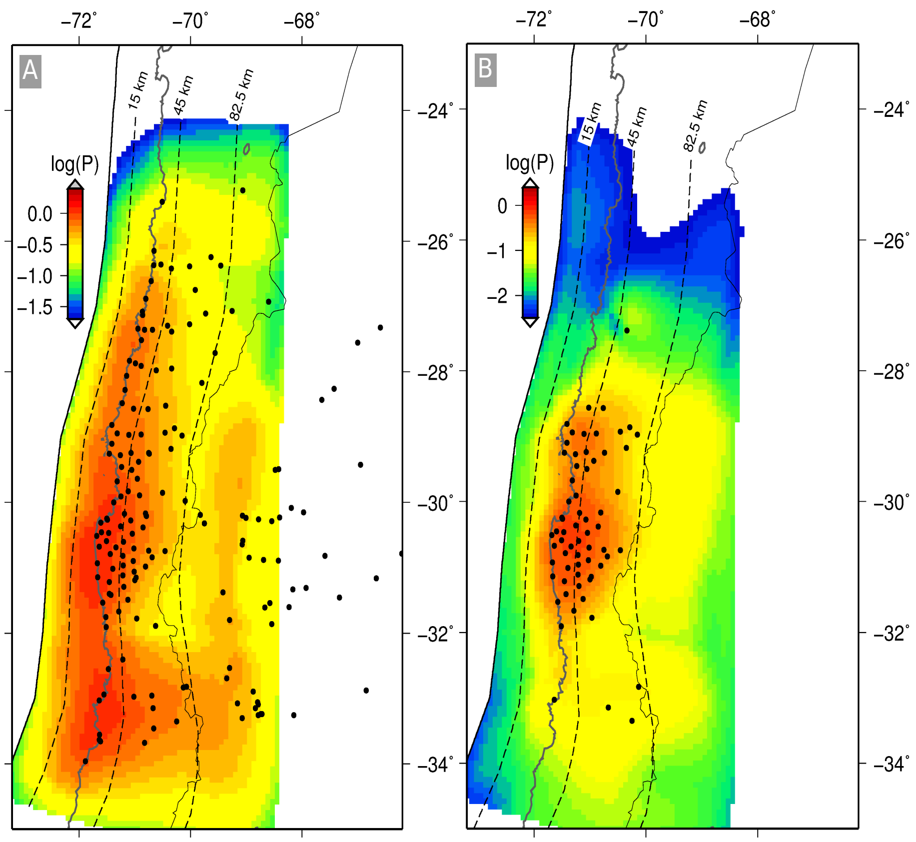

Figure 3: Sensitivity of horizontal (left) and vertical (right) data collected over our network to unit coupling on the 20° dipping slab. Each element of the interface is colored by the log of the sum of the displacements (P in mm/yr) at GPS stations (dots) due to unit slip on the nearest grid node.

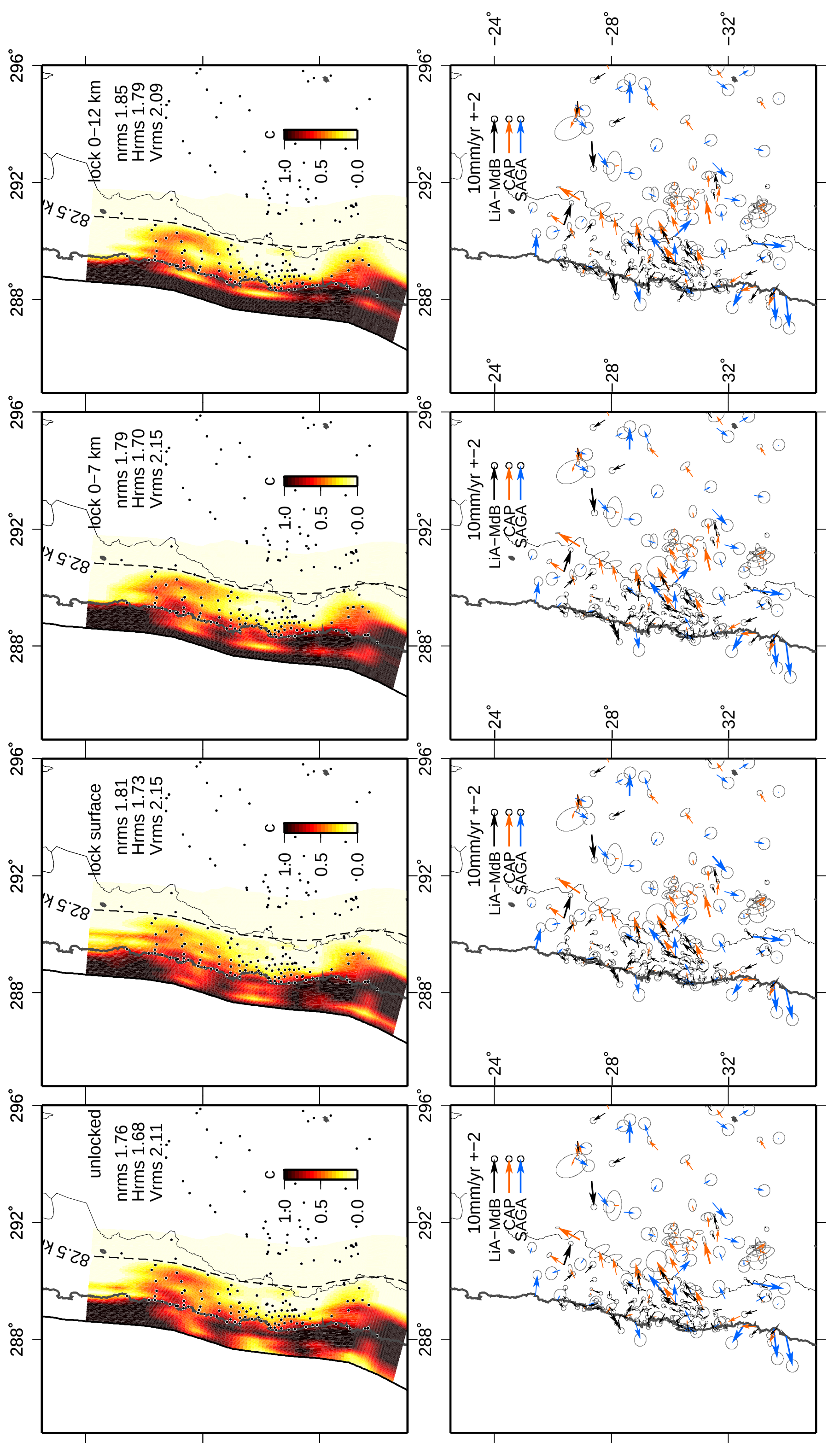

Figure 4: Coupling patterns inverted for a 3-plate model and with different constrains on coupling at shallow depth. The smoothing coefficient is fixed to 0.7/°, and no coupling is allowed under 80 km depth. From left to right : no constrain on shallow coupling, locking of the surface node only, locking of the whole interface from 0 to 7km depth, locking of the whole interface from 0 to 12 km depth. The normalized root mean square (nRMS) is indicated in the upper right corner of each plot.

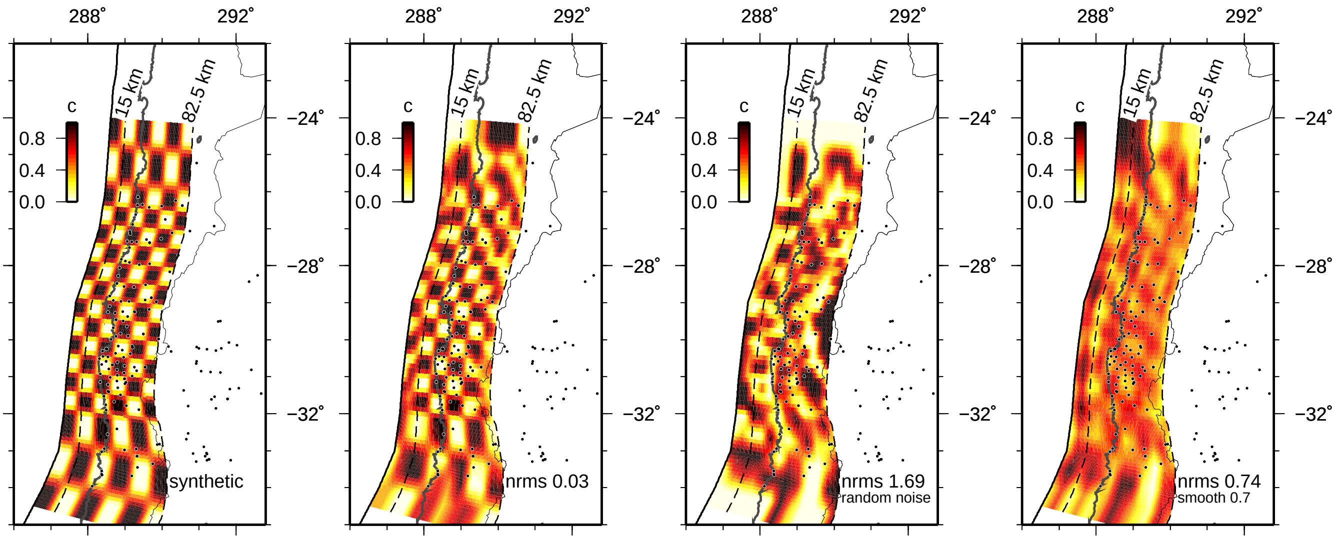

Figure 5: Checkerboard resolution tests. From left to right : coupling checkerboard pattern used to generate a synthetic deformation field; coupling distribution retrieved by an inversion of the raw synthetic velocities without smoothing constrain; coupling distribution retrieved by the inversion of the synthetic velocity field in which random noise (±2 mm/yr in average) has been added; same but adding an increasing with depth smoothing constrain (0.7/°) which smears the small scale original checkerboard.

smoothing in the along-dip direction since it was not implemented in the 2007 Defnode version. Thus we have small variations in the amount of coupling in the same column of nodes that are artifacts of the modeling process.

We plot the normalized RMS associated to data versus roughness amount (i.e. the opposite of smoothing) in supp. Figures 6 and 8 for instance. We also combine the increasing smoothing option with the Defnode down-dip decrease option (or "ddc") that constrain the coupling coefficient to decrease with depth along one column of nodes. We tested several initial values for this smoothing constrain (see figures 6, 7, 8, and 9) and conclude that the 0.7/° surface smoothing yields the best compromise between smoothing and RMS (i.e no significant improvement of the RMS is obtained using rougher solutions).

3.4 Nazca-South America relative motion

The direction and amplitude of the Nazca-South America convergence motion have been extensively debated for years (e.g Norabuena et al., 1998; DeMets, 1994; Kendrick et al., 2003; Vigny et al., 2009). This uncertainty is mainly due to the non-negligible discrepancy that exists between the geological velocity calculated by the Nuvel 1-A model for the Nazca plate (DeMets, 1994) and the ones derived using present-day GPS measurements (Norabuena et al., 1998; Kendrick et al., 2003; Vigny et al., 2009). Both calculations lead to velocities that differ by nearly 15%. This could be the result of a decrease in the convergence velocity between both plates since 3 Myr. The more recent "geological" model using a shorter time span of 0.76 Myr (MORVEL, DeMets et al., 2010) falls halfway between Nuvel 1-A and GPS values (Altamimi et al., 2011) and concur with this idea of a progressive slowing down of the convergence. We summarize in table 7 some of the poles that have been proposed to describe the Nazca-South America motion.

In our modeling, we do not invert for the relative motion between Nazca and South American plate. In our best models, we chose to use the pole calculated by Vigny et al. (2009) using GPS

Model	source	rotation pole (N,E,°/Myr)	⟨velocity⟩ (mm/yr)
Nuvel 1-A	(DeMets, 1994)	56.0 -94.0 0.720	80.0
MORVEL	(DeMets et al., 2010)	54.9 -98.0 0.666	73.9
GPS1	(Norabuena et al., 1998)	47.4 -93.7 0.624	68.3
GPS2	(Kendrick et al., 2003)	61.0 -94.4 0.570	63.3
GPS3-this study	(Vigny et al., 2009)	55.9 -95.2 0.610	67.8
ITRF 2005	(Altamimi et al., 2007)	53.9 -87.5 0.605	67.0

Table 7: Summary of published poles for the Nazca-South America relative motion using either geological methods (top) or GPS velocities only (bottom). The average velocity predicted by each pole at 30°S (i.e the center of our study area) is indicated in the last column (in mm/yr).

measurements in central Chile (55.9°N, 95.2°W, 0.610 °/Myr) that is quite similar to the ITRF rates (±1mm/yr) and slightly lower than the MORVEL rate (-6mm/yr). Because a trade-off exists between the value of the convergence between both plates and the amount of coupling on the subduction interface, we tested the impact on our inversion of using the MORVEL and ITRF 2005 alternative poles (see Alternative models section).

4 Alternative models

We use the subset of alternative models that fit the data with a nRMS better than 2.0 for the 3-plate model and 2.8 for the 2-plate models, to define the uncertainty on the along strike variations of the average coupling $\langle \Phi \rangle$ in figure 6. First, we used the "down-dip decrease" option of the DEFNODE code to constrain the coupling coefficient to decrease with depth (McCaffrey, 2007), in order to get the very first order of the coupling distribution for both the 2-plate and 3-plate models (supp. Figures 7 and 9). We also use the 2-plate and 3-plate models inverted using varying smoothing coefficient presented in Figure 6.

In general, as shown in figure 5 of the main text, whatever the sliver motion or the smoothing coefficient used in the inversion, the lateral variations of the coupling coefficient on the subduction interface are similar. Overall, the 2-plate models show higher and deeper coupling than the 3-plate models, in particular north of Choros (29°S) where our GPS network is sparser and where the motion of the sliver is thought to be higher. The most robust feature seen in both the 2-plate and 3-plate alternative models is the clear decrease in coupling over the large La Serena bay (30°S) located in between two highly locked areas (the Metropolitan area to the South, and the Choros area to the North).

The 3-plate alternative models presented in figures 8 and 9 exhibit similar coupling distributions with some changes in the average coupling depending on the smoothing coefficient imposed due to its influence on the inversion of the sliver motion. Overall, the lateral variations in the coupling distribution remain stable. However, the roughest models show some high coupling patches in the poorly defined deep region of the interface, North of 28°S. This is unclear whereas this patchy coupling distribution is really required by the data. In this case, this would suggest either deep coupling on the interface, potential accumulation of elastic deformation in an unidentified crustal fault, or regional viscous deformation.

smoothing	constrain	NRMS	rotation pole (N,W,°/Myr)	$\langle V \rangle$ (mm/yr)
0.3		1.89	-38.30 62.66 -0.33	5.93
0.5		1.82	-37.56 62.80 -0.33	5.61
0.7		1.76	-39.22 61.51 -0.25	5.28
0.9		1.74	-38.96 61.77 -0.26	5.19
0.7	lock1	1.89	-38.42 61.13 -0.26	5.40
0.7	lock2	1.92	-38.95 61.01 -0.25	5.19
0.7	lock3	1.98	-35.65 63.80 -0.41	5.69
0.3	ddc	1.99	-39.12 62.20 -0.35	6.68
0.5	ddc	1.86	-42.45 58.45 -0.21	5.57
0.7	ddc	1.82	-41.93 55.72 -0.20	5.34
0.9	ddc	1.81	-47.28 52.35 -0.13	5.06

Table 8: Normalized RMS, Andean sliver pole and average horizontal motion produced by block rotation on our network, depending on the constrains imposed in each 3-plate model tested.

The alternative models obtained in the 3-plate configuration allow us to estimate the variability of the inverted rotation pole for the Andean sliver at these latitudes (table 8). We find that the rotation pole is located in a quite narrow area located in the South Atlantic ocean, in the vicinity of the 'Malouines" islands, and that the rotation motion around it produces 5-5.5 mm/yr of deformation in average in our network, with a slight decrease of 2mm/yr from North to South of our network. However, it is

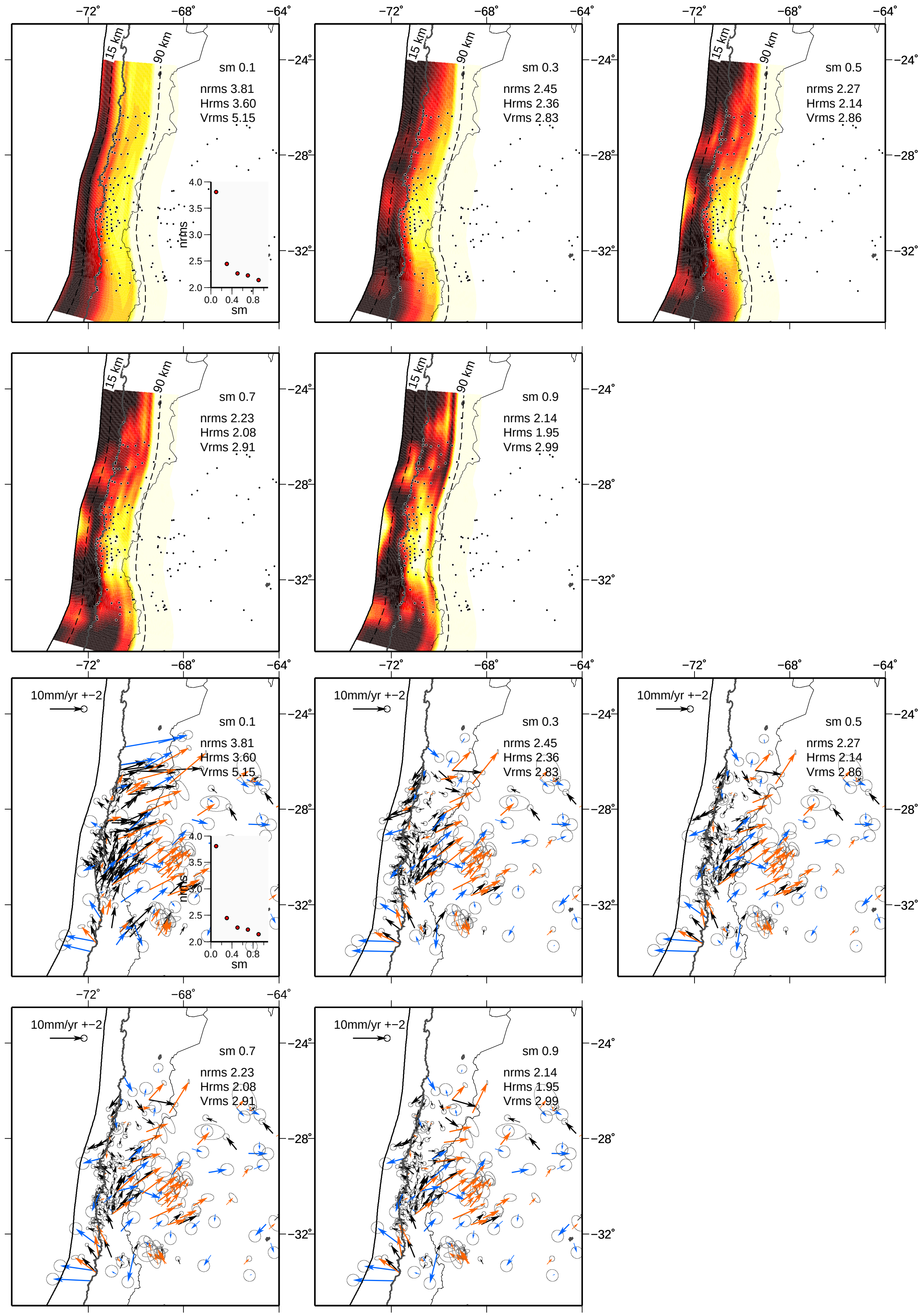

Figure 6: **2-Plate model / varying smoothing values** Coupling patterns inverted using different initial smoothing values. Coupling is color coded as in Figure 5. The smoothing value and the normalized root mean square relative to horizontal (hRMS) or vertical (vRMS) data are indicated in the upper right corner of each plot. We plot the variations of nRMS with smoothing in the bottom right corner of the smoothest inversion

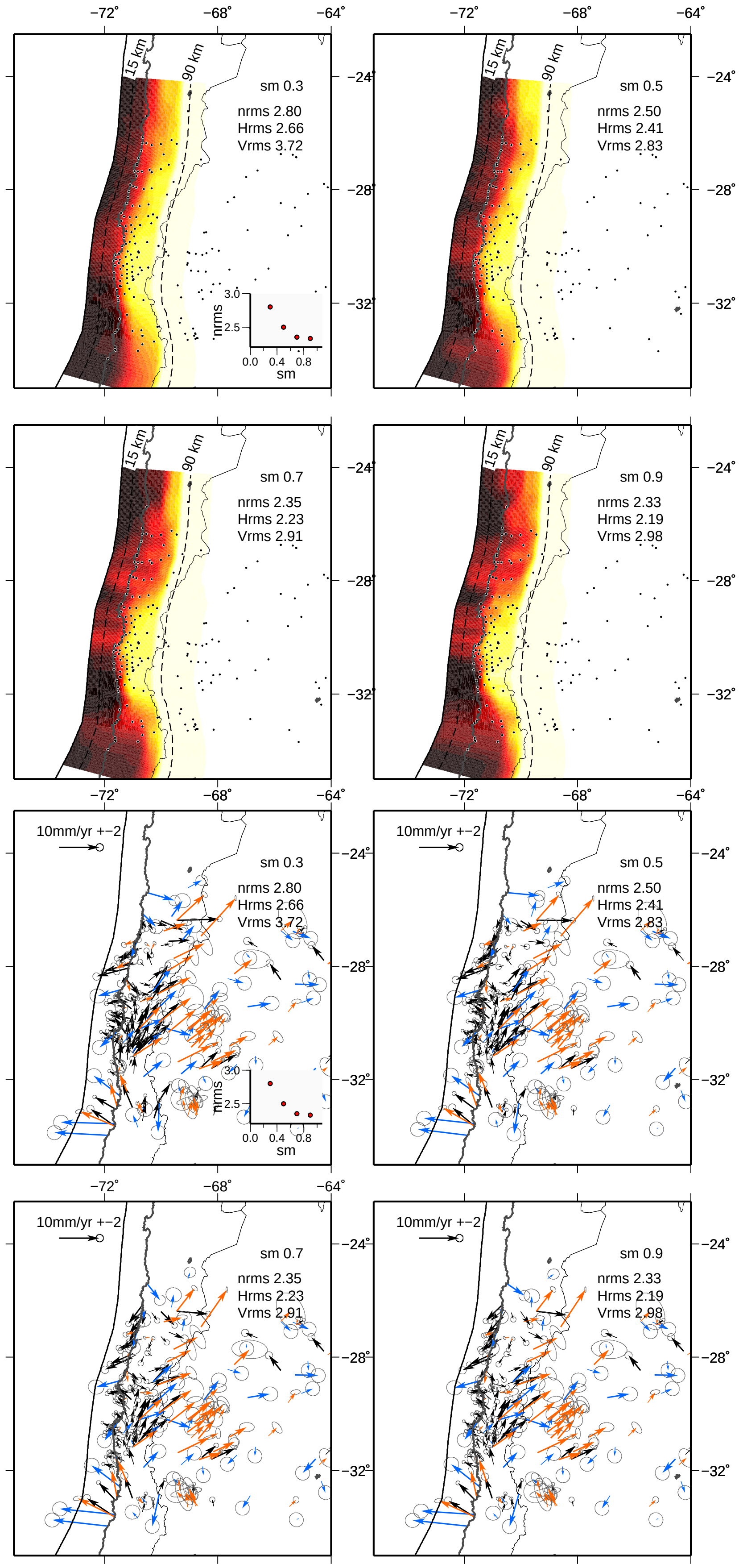

Figure 7: **2-Plate model / varying smoothing values / ddc constrain** Same caption as figure 6, but with “ddc” constrain that forces coupling to decrease with depth.

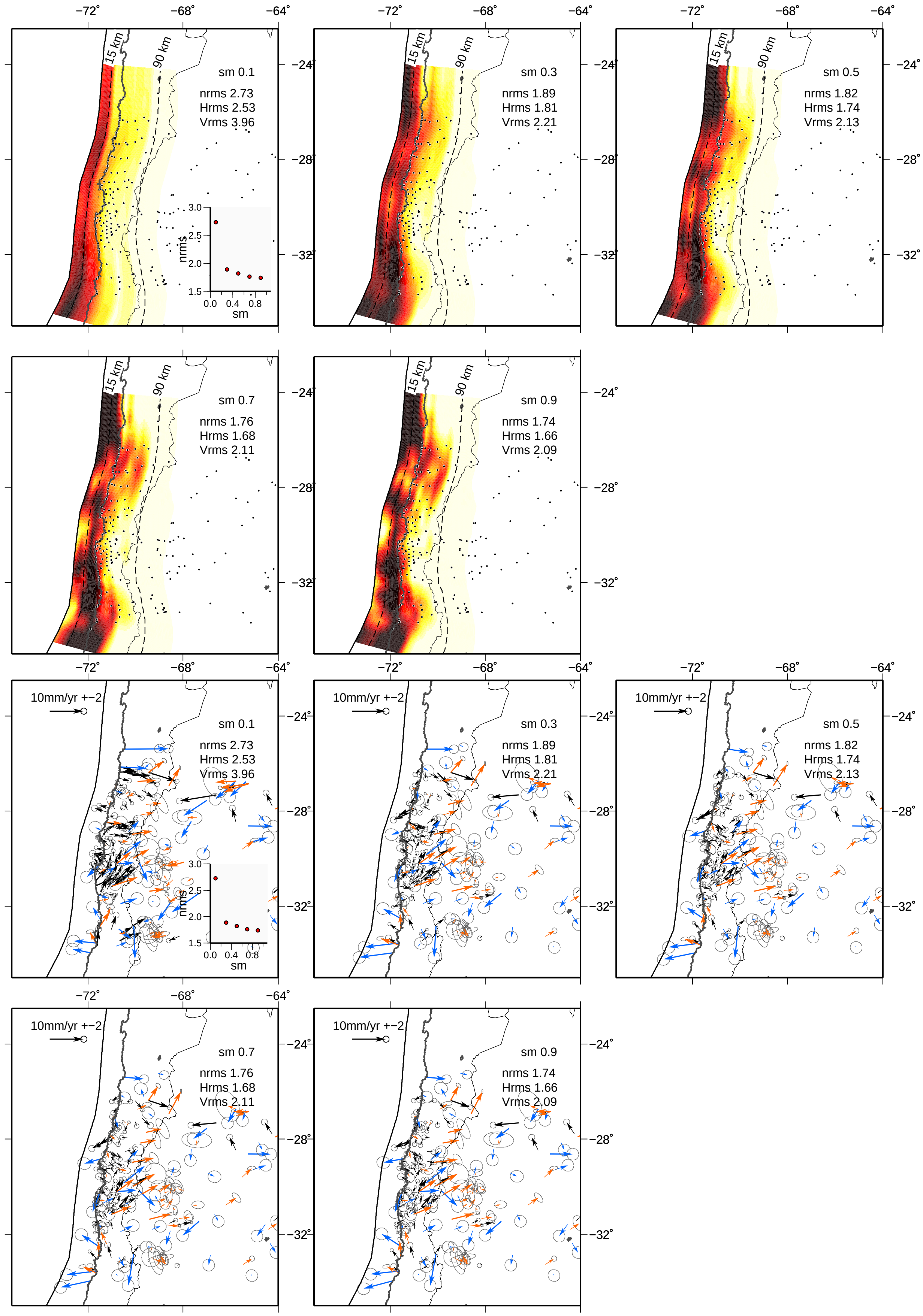

Figure 8: **3-Plate model / varying smoothing values** Same caption as figure 6 but for 3-plate models. The sliver poles found for each inversion are listed in table 8.

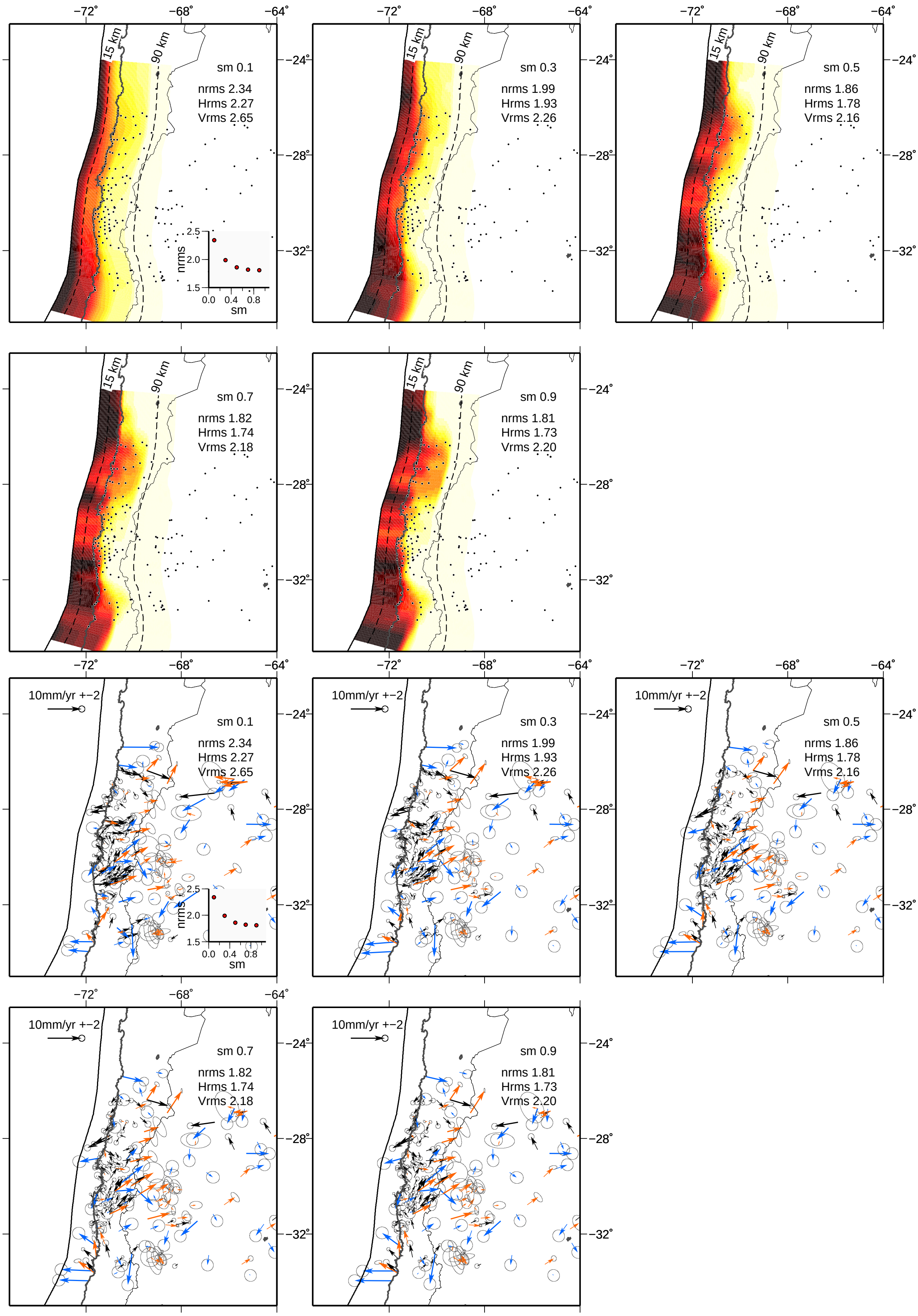

Figure 9: **3-Plate model / varying smoothing values / ddc constrain** Same caption as figure 8, but with “ddc” constrain that forces coupling to decrease with depth.

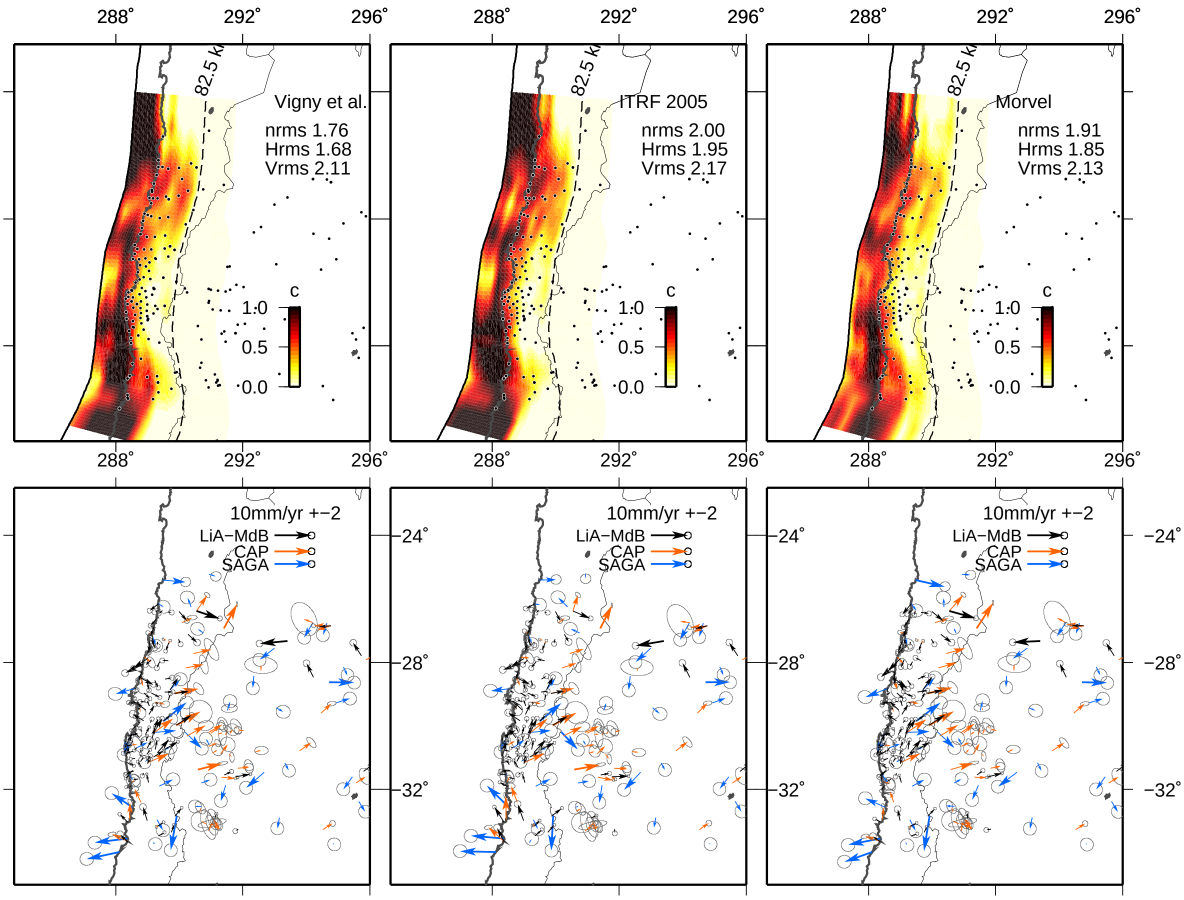

Figure 10: Coupling distribution inverted using various Nazca-South America convergence velocities, with 0.7/° smoothing coefficient that increases with depth, no coupling allowed under 80 km depth, in a 3-plate configuration. From left to right : coupling distribution obtained with increasing relative velocities described by the ITRF 2005, Vigny et al. (2009) and MORVEL (DeMets et al., 2010) poles.

to note that we do not invert for the relative motion between Nazca and South American plate in our modelling procedure.

4.1 Influence of relative plate motion on coupling distribution

In our best models, we chose to use the pole calculated by Vigny et al. (2009) using GPS measurements in central Chile (55.9°N, 95.2°W, 0.610 °/Myr) that is quite similar to the ITRF rates (±1mm/yr) and slightly lower than the MORVEL rate (-6mm/yr, see table 7). The impact of chosing one of these pole to describe the relative motion of Nazca and South American plates has been explored in Métois et al. (2013) for instance, and seems negligible. Figure 10 presents the coupling distributions inverted using three different NazcaSouth-America relative poles. We find that fixing the rotation between Nazca and South-American plates to a higher or lower convergence rate than ~68 mm/yr (estimated from Vigny et al. (2009)) does neither change the details of the coupling distribution on the subduction interface, nor the amount and direction of the inverted sliver motion (see table 9). In particular, the lateral variations of the coupling are very similar: this gives us confidence in the fact that the lateral segmentation is a stable feature. However, logically, we observe that the slower the convergence, the higher the inferred average coupling and the deeper the highly coupled zones.

Pole used	⟨convergence⟩ (mm/yr)	NRMS	sliver rotation pole (N,E,°/Myr)	⟨rot⟩ (mm/yr)
Vigny et al. (2009)	67.8	1.76	-39.22 61.51 -0.25	5.28
ITRF 2005	67	2.00	-37.35 300.05 -0.27	6.05
MORVEL	73.8	1.89	-40.10 297.67 -0.25	5.22

Table 9: Average convergence between Nazca and South America, normalized RMS, Andean sliver pole and average horizontal motion produced by block rotation on our network, depending on the Nazca-South American relative pole imposed in our 3-plate models (figure 10).

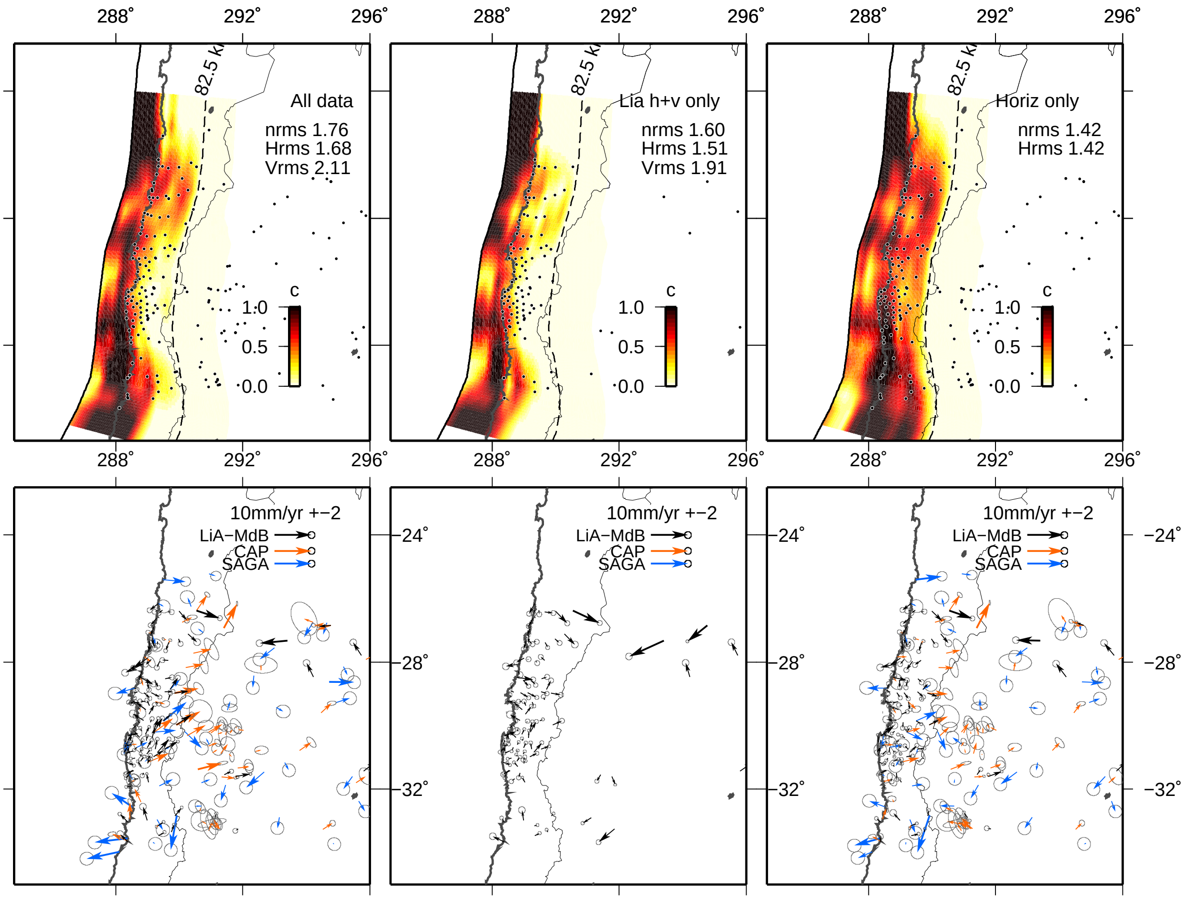

Figure 11: Coupling distribution inverted using different data sets, with 0.7/° smoothing coefficient that increases with depth, no coupling allowed under 80 km depth, in a 3-plate configuration. From left to right : coupling distribution inverted using all available horizontal and vertical velocities, same but using only the more recent data set published in this study (LiA-MdB), coupling distribution inverted using all available horizontal velocities only.

4.2 Influence of vertical and horizontal data sets

As described in the “Detail of GPS data set” section of this supplementary material, we inverted jointly old and recent horizontal data sets together with vertical velocities acquired since 2004. We tested the impact of including these new vertical velocities in the inversion in figure 11 by comparing the coupling distribution obtained by the joint inversion of horizontal and vertical data (i.e. our preferred model) and the one obtained using horizontal velocities only. Again, the lateral variations of the coupling coefficient are stable whatever the data set used, but we can see strong variations in the indepth extent of the highly coupled zones. Inverting both horizontal and vertical velocities leads to a shallowing of the highly coupled zone on the subduction interface and to a narrowing of the downdip transition zones. This is consistent with the fact that vertical velocities are mainly sensitive to the downdip extent of coupling and to the width of the transition zone between highly coupled and freely creeping portions of the interface.

We also inverted the coupling distribution on the subduction interface using only recent GPS data, i.e. the so-called "LiA-MdB" data set acquired from 2004 to 2012 in this region, including vertical and horizontal data (figure 11). The obtained coupling distribution is very similar to the one obtained using all available data in the region. The major difference lays in the sliver motion inverted in both models. Without using the far-field horizontal velocities provided by the old CAP and SAGA data sets, the sliver motion is poorly constrained and the best rotation pole inverted by Defnode in this case (2.77°W, -61.33°S, -0.12°/Myr) produces $\sim$9 mm/yr of eastward motion on average over our network. This important eastward motion is neither consistent with the geological and paleomagnetic studies (e.g. Arriagada et al., 2008) nor with the small current day instrumental seismicity. Therefore, we think that the oldest CAP and SAGA data sets are useful to precisely determine the global motion of the Andes but that they contribute less to the determination of the coupling distribution on the interface.

References

Altamimi,Z., X. Collilieux, J. Legrand, B. Garayt, and C. Boucher. ITRF2005: A new release of the International Terrestrial Reference Frame based on time series of station positions and Earth Orientation Parameters. *Journal of Geophysical Research*, 112(B9):B09401, 2007. ISSN 0148-0227.

Altamimi, Z., Xavier Collilieux, and Laurent Métivier. Itrf2008: an improved solution of the international terrestrial reference frame. *Journal of Geodesy*, 85(8):457–473, 2011.

Arriagada, C., P. Roperch, C. Mpodozis, P. Cobbold, et al. (2008), Paleogene building of the Bolivian Orocline: Tectonic restoration of the central Andes in 2-D map view, *Tectonics*, *27*(6), TC6014

Brooks, Benjamin a. Crustal motion in the Southern Andes (26°âĂŞ36°S): Do the Andes behave like a microplate? *Geochemistry Geophysics Geosystems*, 4(10):1–14, 2003. ISSN 1525-2027.

Chlieh M., Perfettini H., Tavera H., Avouac J.P., Remy D., Nocquet J.M., Rolandone F., Bondoux F., Gabalda G., and Bonvalot S. (2011), Interseismic coupling and seismic potential along the Central Andes subduction zone, *Journal of Geophysical Research*, *116*(B12), 1-21.

DeMets, C. et al. Effect of recent revision to the geomagnetic reversal time scale on estimates of current plate motions. *Geophys Res Lett*, 1994.

DeMets, C., Richard G Gordon, and Donald F Argus. Geologically current plate motions. *Geophysical Journal International*, 181(1):1–80, 2010.

Kendrick, E., M. Bevis, R. Smalley, B. Brooks, R. B. Vargas, E. Lauria, and L. P. S. Fortes (2003), The NazcaâĂŞSouth America Euler vector and its rate of change, *Journal of South American Earth Sciences*, *16*(2), 125–131.

Khazaradze, G. Short- and long-term effects of GPS measured crustal deformation rates along the south central Andes. *Journal of Geophysical Research*, 108(B6):1–13, 2003. ISSN 0148-0227.

Loveless, J.P. & B.J. Meade. Spatial correlation of interseismic coupling and coseismic rupture extent of the 2011 mw= 9.0 tohoku-oki earthquake. *Geophys. Res. Lett*, 38:L17306, 2011.

Marot, M., T. Monfret, M. Gerbault, G. Nolet, G. Ranalli and M. Pardo Flat vs. Normal subduction, Central Chile: insights from regional seismic tomography and rock type modeling *EGU General Assembly Conference Abstracts*, 15:5127, 2013.

R McCaffrey. Crustal block rotations and plate coupling. *Plate Boundary Zones, Geodyn. Ser*, 2002.

McCaffrey, R . DEFNODE User's Manual Version 2007.10. 25, 2007. URL `http://web.pdx.edu/ mccaf/www/defnode/defnode_071025.html`.

Métois, M., A. Socquet, and C. Vigny. Interseismic coupling, segmentation and mechanical behavior of the central chile subduction zone. *J. geophys. Res*, 117(B03406), 2012.

Métois, M., A. Socquet, C. Vigny, D. Carrizo, S. Peyrat, A. Delorme, E. Maureira, I. Ortega and C-M Valderas-Bermejo. Revisiting the North Chile seismic gap segmentation using GPS-derived interseismic coupling *in press to Geophys. J. Int.*, 2013.

Norabuena E., Leffler-Griffin L., Mao A., Dixon T., Stein S., Sacks I.S., Ocola L., and Ellis M. Space geodetic observations of Nazca-South America convergence across the central Andes. *Science*, 279 (5349):358, 1998.

Okada, Y. Surface deformation due to shear and tensile faults in a half-space. *Bulletin of the Seismological Society of America*, 1985.

Pardo, M., D. Comte, and T. Monfret. Seismotectonic and stress distribution in the central Chile subduction zone. *J. of South American Earth Sciences*, 15-1(11–22), 2002.

Vigny, C., A. Rudloff, JC. Ruegg, R. Madariaga, J. Campos, and M. Alvarez. Upper plate deformation measured by GPS in the Coquimbo Gap, Chile. *Physics of the Earth and Planetary Interiors*, 175 (1-2):86–95, June 2009. ISSN 00319201.

Vigny, C., A Socquet, S Peyrat, J-C Ruegg, M Métois, R Madariaga, S Morvan, M Lancieri, R Lacassin, J Campos, D Carrizo, M Bejar-Pizarro, S Barrientos, R Armijo, C Aranda, M-C Valderas-Bermejo, I Ortega, F Bondoux, S Baize, H Lyon-Caen, A Pavez, J P Vilotte, M Bevis, B Brooks, R Smalley, H Parra, J-C Baez, M Blanco, S Cimbaro, and E Kendrick. The 2010 Mw 8.8 Maule megathrust earthquake of Central Chile, monitored by GPS. *Science*, 332(6036):1417–21, June 2011. ISSN 1095-9203.